Available online at www.sciencedirect.com

ScienceDirect

Acta Materialia 77 (2014) 269–283

Acta MATERIALIA

www.elsevier.com/locate/actamat

Understanding the mechanical behavior of nanocrystalline Al–O thin films with complex microstructures

Mo-Rigen He [a], Peter J. Felfer [b], Suman Dasgupta [c], Saritha K. Samudrala [e], Patrick J. Malone [a], Gang Feng [d], Kevin J. Hemker [c], Julie M. Cairney [b,e], Daniel S. Gianola [a,*]

[a] Materials Science and Engineering, University of Pennsylvania, Philadelphia, PA 19104, USA
[b] Australian Centre for Microscopy and Microanalysis, University of Sydney, NSW 2006, Australia
[c] Mechanical Engineering, Johns Hopkins University, Baltimore, MD 21218, USA
[d] Mechanical Engineering, Villanova University, Villanova, PA 19085, USA
[e] School of Aerospace, Mechanical and Mechatronic Engineering, University of Sydney, NSW 2006, Australia

Received 26 November 2013; received in revised form 26 May 2014; accepted 29 May 2014

Abstract

The mechanical behavior of nanocrystalline (NC) metals has attracted widespread interest, though the majority of efforts have focused on (nominally) pure metals. By comparison, the mechanisms of deformation and strengthening in NC alloys, especially those with high segregation propensity and strong chemical interactions, are less well understood. Here we present a quantitative investigation on the mechanical behavior of such an alloy system. NC Al–O thin films are synthesized by means of confocal co-sputtering, which enables a wide-range and quasi-independent control over impurity content and grain size. Detailed characterization combining transmission electron microscopy with three-dimensional atom probe tomography identify the multiple morphologies of O impurities in a composite-like microstructure, including nanosized α-Al_2O_3 precipitates, O-rich clusters segregated along grain boundaries, and O solute atoms inside Al grains. Individual contributions of these strengthening features to the mechanical properties of NC Al–O thin films, as measured by instrumented nanoindentation, are then well delineated by a microstructure-informed analytical model. Dislocations emitted from grain boundaries are pinned by the stronger obstacles and cut through the weaker, and we show that the strong chemical interactions of this Al–O system play a dominant role in its pronounced strengthening capability. The influence of O impurities on the plasticity and deformation mechanisms in NC Al films is also discussed based on microtensile testing.

Keywords: Nanocrystalline; Thin films; Alloys; Strengthening mechanisms; Atom probe tomography

1. Introduction

Nanocrystalline (NC) metals have attracted widespread interest due to their outstanding mechanical behavior including high strength [1–4], improved flaw tolerance [5,6], and high resistance to corrosion [7], fatigue [8] and wear [9]. However, the mechanisms governing plastic deformation and strengthening in NC metals have not been fully explored on a quantitative level. While some experiments have shown that the conventional Hall–Petch (H–P) relationship can be extrapolated from the coarse- and ultrafine-grained regime to grain sizes as small as 10–20 nm [2,10–12], more recent studies by means of in situ testing [6,13–23] and atomistic simulations [10,24–29] have underlined the emergence of new deformation mechanisms at reduced size scale. These include twinning/detwinning [13,22], dislocation emission/absorption at grain boundaries (GBs) [14,21,24,26], GB sliding [10,27–29],

* Corresponding author. Tel.: +1 2158987974.
E-mail address: gianola@seas.upenn.edu (D.S. Gianola).

http://dx.doi.org/10.1016/j.actamat.2014.05.058
1359-6454/

grain rotation [15,25], GB migration [16,27] and stress-coupled grain growth [15–20], which provide new prospects for tailoring the mechanical properties of NC metals.

However, most studies to date have focused on (nominally) pure NC metals. As a classic strengthening strategy in bulk structural materials [30], alloying is also expected to play a prominent role in governing the microstructure and mechanical properties of NC metals. It has been recognized that GB migration can be retarded by solute atoms, either through the kinetic drag effect [31] or by the reduction of GB energy due to solute segregation along GBs [32,33]. A more refined model to predict the thermodynamic stability of NC alloys based on the free energy of mixing was recently proposed by Schuh et al. [34,35]. Consequently, NC alloys can be adequately stabilized against thermal grain growth, thus retaining their fine grain size and concomitant high strength [36,37]. The mechanical stability of NC alloys [38,39], in contrast, has received much less attention despite many reports of stress-driven grain growth in (nominally) pure NC metals [15–20]. In one study, Tang et al. confirmed the segregation of O atoms at GBs of NC Al thin films by using three-dimensional atom probe tomography (3D-APT) [40], and showed that the GB excess of O increased with the base pressure of sputtering deposition [41]. Additions of O also led to the suppression of stress-driven grain growth, accompanied by a transition of tensile behavior of the freestanding NC Al thin films [18] from "ductile and moderately strong" to "very strong and brittle", which qualitatively corroborated atomistic simulations by Elsener et al. [42] showing that the critical stress for coupled GB migration increased with the GB excess of impurity atoms. Beyond these studies of nanostructural stability, the applicability of classic strengthening models (i.e. based on dislocation–obstacle interactions) in NC alloys remains an open question. To this end, Rupert et al. [43] recently proposed a new mechanism for solid–solution strengthening of NC alloys. By combining the classic Fleischer model [44] with the GB-pinning effect of dislocations, which was augmented by a modification of global lattice properties due to alloying, the strengthening behavior of their Ni–W alloys as well as several other NC alloys were well described.

Experimentally, alloy strengthening of NC thin films has mainly focused on metal–metal binary systems including Cu–Fe [45,46], Cu–Nb [46], Ni–Cu [45], Ni–W [11,44], Al–Fe [47] and Al–Mo [48]. Taken as a whole, the effectiveness of strengthening was found to increase with segregation energy and the size misfit between solute and solvent atoms [49]. However, the strengthening behavior of NC alloy systems with both high segregation propensity and strong chemical interactions, such as Al–O [42] and Ni–P [50], is still far from understood. Systematic investigations of this type of NC alloys have special significance due to their extraordinary effectiveness for grain size refinement [34] and strengthening, thus serving as promising candidates for applications such as wear-resistant coatings [51,52] and oxide-dispersion-strengthened alloys [53,54]. On the other hand, quantitative modeling of the impurity strengthening mechanisms in these complex microstructures also faces special difficulties, as the cooperation between the multiple strengthening features, including but not limited to solute atoms, precipitates and GBs, requires a thorough characterization of both spatial distribution and chemical states of the impurities. However, atomistic simulations are of limited assistance in this regard since accurate interatomic potentials with strong charge-transfer characteristics are still relatively immature [42]. In addition, convolution of the strengthening effects coming from impurity and grain size, a common and elusive issue in NC alloys [45,48], also needs to be addressed. Accurate control of impurity content through film deposition is another practical issue (at least for the Al–O system), since the previous route of changing base pressure [41] showed only limited control of impurity content and species.

In the present study, NC Al–O thin films were synthesized by means of co-sputtering, which enables wide-range and quasi-independent control over impurity content and grain size. By using transmission electron microscopy (TEM) combined with 3D-APT, the multiple morphologies of O are identified in a complex composite-like microstructure, and their strengthening contributions to the mechanical properties of NC Al–O thin films, as measured by instrumented nanoindentation, are distinguished based on an analytical model. The influence of O impurities on the deformation mechanisms of NC Al films is also discussed based on microtensile testing.

2. Materials and methods

NC Al thin films with varied O content were synthesized by magnetron co-sputtering in an Explorer 14 sputtering system (Denton Vacuum). A 99.999% pure Al target and a 99.995% pure α-Al_2O_3 target were configured in confocal geometry, and the chamber stage was rotated to maintain uniformity of film thickness and composition. The Al target was sputtered by DC powers of 200 and 300 W, whereas the RF power on the α-Al_2O_3 target was varied from 0 to 150 W, yielding 12 deposition batches with 8 different DC/RF power combinations: 200/0, 200/10, 200/50, 200/100, 300/0, 300/15, 300/75 and 300/150. Hereinafter, all batches are referred to by their DC (the first number) and RF (the second number) powers in Watts. For each batch, NC Al–O thin films were deposited on Si(100) with the native oxide layer intact [55], fused silica glass and Cu TEM grids with supporting C films. The chamber was evacuated to $\sim 4 \times 10^{-7}$ Torr and then filled with Ar gas flow at 25 sccm. Deposition was performed at a chamber pressure of $\sim 5 \times 10^{-3}$ Torr. Deposition rates (for each DC power) were calibrated beforehand so that similar film thicknesses (t) of 160–180 nm were achieved for most batches.

For each batch, global O content (C_O) was measured in the films deposited on Si(100) by using energy-dispersive spectroscopy (EDS) in an FEI Quanta 600 scanning electron microscope (SEM) operated at 10 kV. Plan-view

TEM characterization (bright-field imaging, dark-field imaging and selected-area electron diffraction) were performed in a JEOL 2100 for the films directly deposited on Cu grids, and grain size statistics were carried out based on the area-equivalent circular diameters [43] of over 1000 grains, which were manually traced out from dark-field images. Cross-sectional TEM specimens were cut and lifted out from selected batches of films deposited on Si(1 0 0) by using a focused ion beam (FIB, FEI Strata DB235) operated at 30 kV (an ion beam current of 30 pA was used for fine milling), and subsequently transferred to a Cu TEM grid using a MM3A micromanipulator (Kleindiek Nanotechnik). High-resolution TEM (HRTEM) imaging for the cross-sections was then performed using a JEOL 2010F.

For the preparation of atom probe specimens, similar cross-sections were transferred to an electropolished Mo TEM grid [56] in a FEI Quanta 200 3D FIB/SEM. The growth direction of films was oriented perpendicular to the axis of Mo tips, which maximized the volume of films that can be captured. Fine milling was then carried out in a Zeiss Auriga FIB/SEM using a low-energy (5 kV) ion beam in order to minimize Ga implantation [56]. Atom probe data were acquired using a Cameca LEAP 4000X Si operated in voltage pulsing mode at 40 K, with pulsing voltage being 20% of DC bias voltage. The evaporation rate was kept at 1% of the pulsing rate of 200 kHz for all experiments. Data reconstruction and visualization were performed using the protocol by Geiser et al. [57] and 3Depict software [58]. O^+, AlO^+ and minor amounts of O_2^+, O^{2+}, AlO^{2+}, AlO_2^+ and AlO_2^{2+} were identified in the mass spectrum as O-containing species, which were used for the visualization of O distribution. The O contents in atom probe specimens were also measured and (when applicable) compared with the global C_O measured by EDS. Analysis of O distribution was facilitated by means of Voronoi volume distribution through custom MATLAB (Mathworks Inc.) programs [59].

The mechanical properties of NC Al–O thin films were measured by instrumented nanoindentation for each batch of films deposited on glass substrates, which provide the lowest elastic mismatch with the films, thus simplifying the extraction of intrinsic film properties [60]. Continuous stiffness measurements (CSM) [61] were carried out using an Agilent G200 with DCM II module and a diamond Berkovich tip. All tests were performed using constant indentation strain rates ($\dot{\varepsilon}_i = \dot{h}/h$, where h is indentation depth) modulated with a small (<1 nm) displacement oscillation at 50 Hz. The maximum indentation depth was 450–500 nm, which was more than twice t. The Saha–Nix method [60] was applied to calculate the "true" indentation hardness of films. Each data presented is averaged from at least 16 indentations.

Microtensile testing was also carried out for selected batches of films using a custom-built system, as previously described in detail [62]. First, microtensile-bar arrays were patterned on negative photoresist (Futurrex NR9-3000PY, thickness ~3 μm) spun on a Si wafer, and NC Al–O thin films were deposited on the photoresist layer (alongside the other substrates mentioned above). The microtensile-bars were then lifted off in acetone and transferred to polypropylene microframes. The side-strips of these microframes were easily burnt away with a soldering iron after mounting and alignment, leaving the freestanding microtensile-bars, which were then uniaxially loaded at a constant strain rate of $4 \times 10^{-5}\,s^{-1}$. Load was directly measured from a 100 mN load cell (with 0.1 mN load resolution), and strain was measured in the gauge section using digital image correlation (with 10^{-5} strain resolution) of the optical microscopic images recorded during testing [62].

3. Results

3.1. Microstructural characterization

Table 1 lists the thickness, composition, grain size statistics and mechanical properties of all batches of NC Al–O thin films; the detailed measurement process is presented in this section. Consistent microstructure (and thus mechanical properties) was confirmed and can be expected for the same batch of films deposited on different substrates, in view of the similar amorphous nature of all substrate surfaces [55]. A series of bright-field TEM images (Fig. 1) shows the plan-view microstructure of NC Al–O thin films, which substantially varied with DC/RF powers, and Fig. 2a,b show representative electron diffraction patterns. Quasi-continuous diffraction rings composed of discrete spots from face-centered cubic (fcc) Al were revealed for all batches of films, with no evidence of strong in-plane or out-of-plane texture. The absence of (or weak) texture has also been reported in some NC Al [18,55] and in certain alloyed [43,63] thin films sputtered on amorphous substrates. In addition, a few extra spots, which were indexed as α-Al_2O_3 using the fcc-Al rings as an internal reference, were seen in all co-sputtered films. Even the nominally pure 200/0 and 300/0 films (RF power turned off) were no exception, though with far fewer extra spots observed, which may result from residual O in the chamber and the strong chemical interactions of the Al–O system. This composite microstructure was further revealed via grain size statistics as measured from dark-field TEM images. Rather than common log-normal distribution, the representative grain size statistics shown in Fig. 2c and d were more accurately fitted by the superposition of two log-normal distributions, as indicated by the strongly asymmetric profile in logarithmic coordinates. Indeed, the two separate distributions arise from respective contributions of Al grains and α-Al_2O_3 precipitates, as shown below. Therefore, the mean grain size ($\langle d_{Al}\rangle$) is hereinafter defined as the larger average size of the two distributions.

Fig. 3 plots $\langle d_{Al}\rangle$ vs. C_O for all batches of films. For a fixed DC power, it is evident that $\langle d_{Al}\rangle$ decreased and C_O increased with increasing RF power. Similar grain size refinement by impurities has been extensively observed in

Table 1
Summary of NC Al–O thin films: target powers, film thickness, composition, grain size statistics, and mechanical properties determined by nanoindentation and microtensile testing (see text for details).

DC/RF (W)	t (nm)	C_O (at.%)	$\langle d_{Al}\rangle$ (nm)	$\langle d_{NP}\rangle$ (nm)	H_f (GPa)	σ_y (MPa)	UTS (MPa)	ε_f (%)
300/0	180	0.5 ± 0.1	76	10	1.4 ± 0.1			
200/0	184	0.7 ± 0.1	86	10	1.3 ± 0.1	64 ± 4	211 ± 1	4.2 ± 0.2
200/0	156	0.8 ± 0.1	84	9	1.3 ± 0.1	93 ± 18	230 ± 2	1.8 ± 0.5
300/15	180	0.9 ± 0.1	71	9	1.5 ± 0.1			
200/10	180	1.1 ± 0.1	76	8	1.4 ± 0.1			
200/10	122	1.2 ± 0.3	49	9	1.7 ± 0.1			
300/75	210	2.0 ± 0.3	38	11	2.2 ± 0.2			
200/50	187	2.8 ± 0.2	38	10	1.8 ± 0.1	205 ± 11	354 ± 13	1.0 ± 0.1
200/50	206	2.9 ± 0.2	40	9	1.9 ± 0.2	133 ± 14	235 ± 6	2.1 ± 0.4
300/150	210	4.8 ± 0.5	19	7	2.5 ± 0.3			
200/100	178	7.1 ± 0.3	32	8	2.4 ± 0.2			
200/100	170	7.9 ± 0.2	28	13	2.6 ± 0.2			

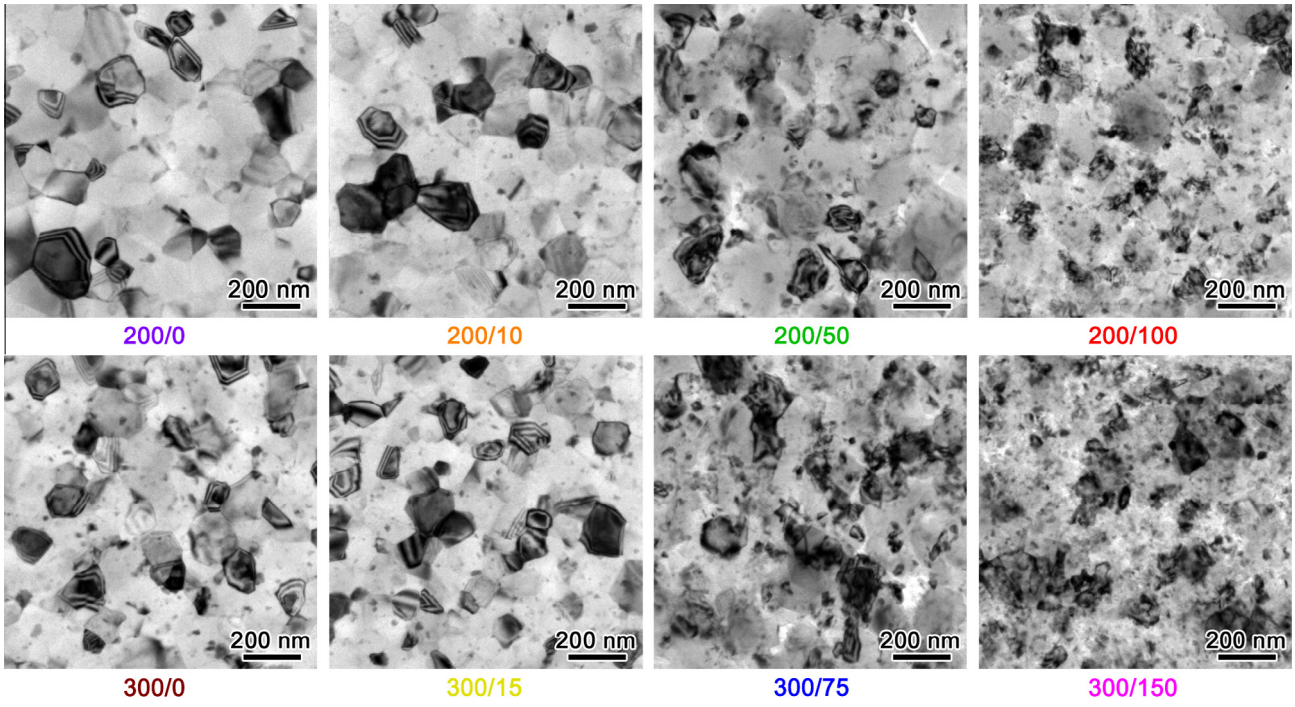

Fig. 1. Bright-field TEM images of co-sputtered NC Al–O thin films using different DC power on Al target (the first number) and RF power on α-Al_2O_3 target (the second number).

NC alloys synthesized by various routes [45,64], while sputtering deposition in far-from-equilibrium conditions has been shown capable of controlling microstructure with an extra degree-of-freedom, i.e. the deposition rate [43,65]. Here we show that for a fixed ratio of DC/RF powers but increasing DC power, $\langle d_{Al}\rangle$ generally decreased (for similar t) due to the increase of deposition rate. Meanwhile, C_O was also found to decrease, presumably because less residual O inside the chamber was incorporated into the films when using shorter deposition times. Overall, the confocal co-sputtering approach employed here has demonstrated the potential for systematic and, more importantly, separate variation of O content and grain size, by combining control of the DC and RF powers on Al and Al_2O_3 targets (see inset of Fig. 3).

The distinct morphologies of O impurities in the composite microstructure of NC Al–O thin films were further revealed by HRTEM characterization of cross-sectional specimens. A low-magnification bright-field image (Fig. 4a) shows the predominance of elongated grains. Typically, several (sometimes single) grains could be found through the film thickness, and further measurements based on dark-field TEM images yielded an averaged aspect ratio (η) of 2.3 ± 0.4 for these Al grains, with the major axis aligned with the growth direction of film. Fig. 4b presents an experimental HRTEM image, and Fig. 4c is the corresponding Fourier transform, in which reflections from both fcc-Al and α-Al_2O_3 can be indexed. The shape and location of these two phases were further highlighted by reflection-filtered inverse Fourier

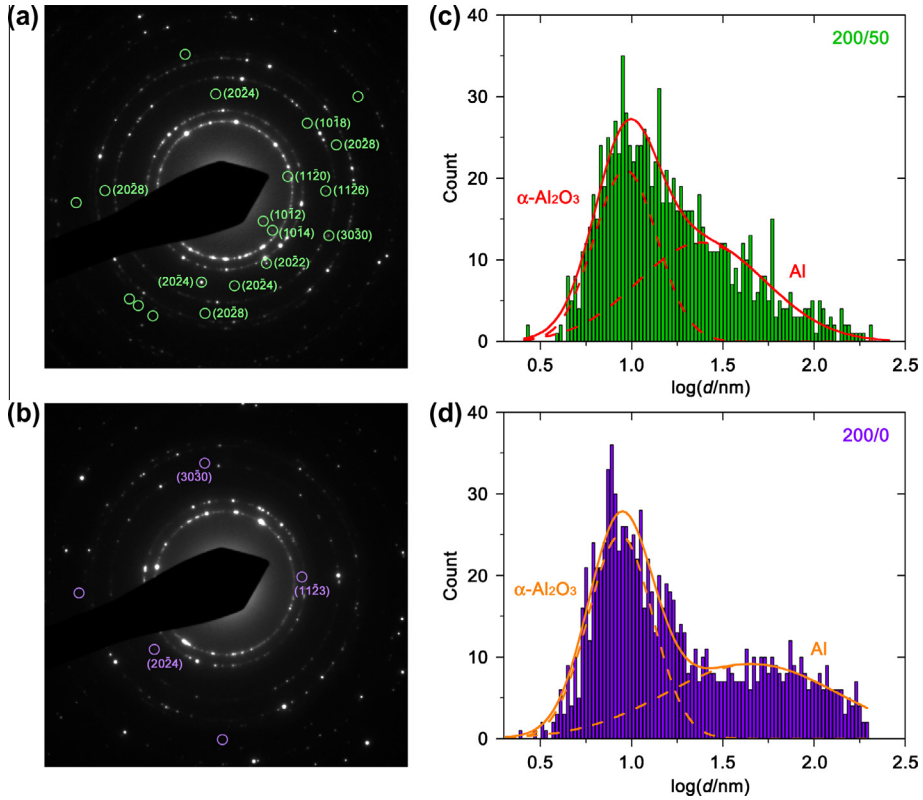

Fig. 2. Selected-area diffraction pattern and grain size statistics of (a and c) the co-sputtered 200/50 film and (b and d) the nominally pure 200/0 film. Extra spots (marked by circles) in (a and b) are mostly indexed as α-Al_2O_3. A few off-center spots are not indexed because there are many planes with similar interplanar spacings. Solid curves in (c and d) are fitted using superposition of two log-normal distributions (shown by dashed curves). (For interpretation of the references to color in this figure, the reader is referred to the web version of this article.)

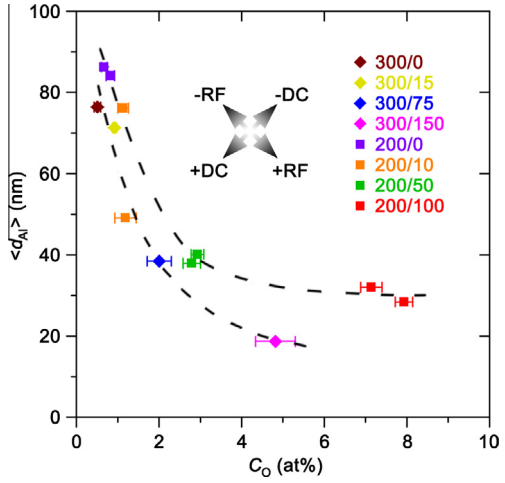

Fig. 3. Variation of global O content (C_O) and mean grain size ($\langle d_{Al}\rangle$) of NC Al–O thin films. Inset arrows show the effects of DC and RF powers on C_O and $\langle d_{Al}\rangle$. Dashed lines (as visual guides) show the trends for each DC power. (For interpretation of the references to color in this figure, the reader is referred to the web version of this article.)

transforms. Whereas the Al grains (e.g. in Fig. 4d) were confirmed to be elongated, the α-Al_2O_3 precipitates (e.g. in Fig. 4e) were mostly spherical. In addition, α-Al_2O_3 precipitates were typically found overlapping with Al grains in HRTEM images, resulting in the secondary diffraction spots frequently observed in Fourier transforms (e.g. the "SD" in Fig. 4c). However, more dedicated characterization (such as electron tomography based on tilt-series HRTEM) would be required to clarify whether α-Al_2O_3 precipitates are located inside Al grains or at GBs. Nevertheless, α-Al_2O_3 precipitates were commonly found in HRTEM images in all examined cross-sectional specimens with different DC/RF powers. Fig. 4f shows that their size statistics followed a log-normal distribution with an average size of 7 nm, qualitatively in accordance with the grain size statistics obtained from plan-view dark-field images, where the distribution with smaller average size was centered at 9 nm (averaging all batches of films, see $\langle d_{NP}\rangle$ in Table 1). Interestingly, the precipitate sizes were largely invariant to C_O and $\langle d_{Al}\rangle$. Thus, we confirmed that the bimodal grain size distribution, as typically shown in Fig. 2c and d, resulted from the composite of Al grains and α-Al_2O_3 precipitates in NC Al–O thin films.

In the above TEM (both dark-field and HRTEM) characterization, the lower size limit for α-Al_2O_3 precipitates that can be clearly identified was ~2 nm, as limited by the intensity of coherent scattering. However, the co-sputtered films presumably contained an abundance of O impurities in other forms with even smaller sizes, such as precipitate embryos containing only a few unit cells [54], O-rich clusters and GB-segregated solute atoms as previously reported [40]. The spatial distribution and chemical states of these O species are also expected to play important

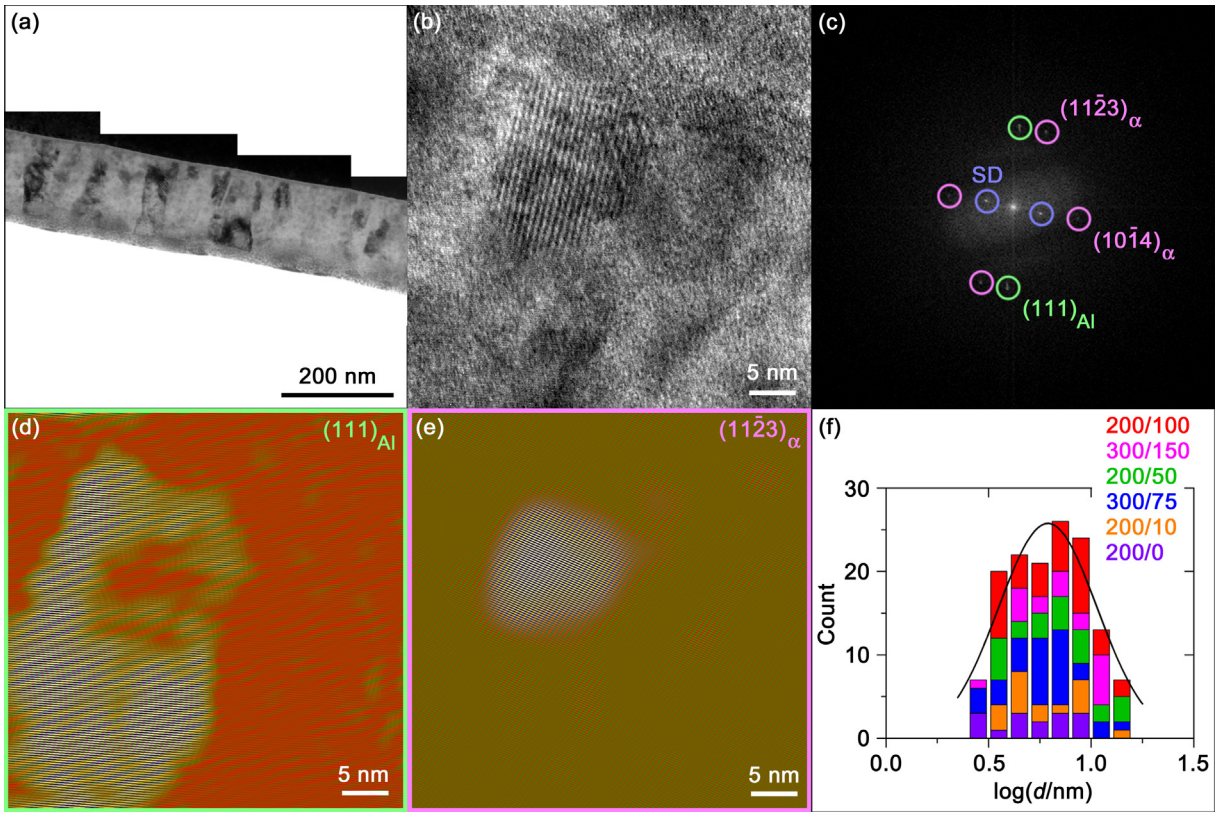

Fig. 4. Cross-sectional TEM characterization of NC Al–O thin films. (a–e) Representative results of the 200/50 film. (a) Low-magnification image. (b) Experimental HRTEM image and (c) Fourier transform of (b). The subscripts Al and α corresponds to reflections from Al grain and α-Al_2O_3 precipitate, respectively. SD is the secondary diffraction between $(1\,1\,1)_{Al}$ and $(1\;\;1\;\;\bar{2}\;\;3)_\alpha$. (d) Inverse Fourier transform of (c) filtered by $(1\,1\,1)_{Al}$. (e) Inverse Fourier transform of (c) filtered by $(1\;\;1\;\;\bar{2}\;\;3)_\alpha$. (f) Size statistics of α-Al_2O_3 precipitates as measured from HRTEM images of different cross-sectional specimens. (For interpretation of the references to color in this figure, the reader is referred to the web version of this article.)

roles in governing the mechanical behavior. To this end, 3D-APT is an ideal technique providing spatial resolution at the atomic scale with concurrent chemical identification of each atomic species [66–68]. Atom probe datasets were obtained from the 200/0, 200/10, 200/50 and 300/75 films, and Fig. 5a shows a representative reconstructed image of a slice with volume of $130 \times 120 \times 8$ nm^3 cropped from a dataset obtained from a 200/50 film. Al, O and Ga atoms are shown as yellow, green and red dots, respectively. Ga atoms are segregated along Al GBs, which is a well-understood artifact of the specimen preparation process by FIB [69,70] and helps to outline the Al grains. In all datasets, no evidence of gradients in grain size was observed through the film thickness. Fig. 5b shows the spatial distribution of O atoms in the same slice as Fig. 5a. However, it is not obvious from simple visualization of the dataset whether there is an increase of O content near the GBs as outlined by the Ga atoms. To this end, the segregation of O atoms was further investigated by means of Voronoi volume (V_V) distribution analyses [59], which highlighted the localized variation of O concentration. Fig. 5c shows the experimental V_V distribution of all O atoms in the 200/50 film dataset ($f_{EXP}(V_V)$), the calculated V_V distribution of the same number of randomly distributed O atoms ($f_{RND}(V_V)$), as well as their difference, indicating that O atoms were indeed not uniformly distributed in our films. Based on this, the extra O atoms that belong to regions with $V_V \leqslant V_{V0}$, which is the first zero point of $f_{EXP}(V_V)$–$f_{RND}(V_V)$, and equivalently with O concentration higher than a threshold level, were picked out and classified as O-rich clusters, while the remaining O atoms were considered as random solutes (see Fig. 5c, and more details in Ref. [59]). Their spatial distributions in the same slice as Fig. 5a are shown in Fig. 5d and e. This visualization confirms that the solute atoms were quite uniformly dispersed throughout the specimen. In contrast, the O-rich clusters were mostly present in the vicinity of GBs. Fig. 5f further shows the size (N) distribution of O-rich clusters in the dataset of 200/50 film. Only the O-rich clusters larger than a cutoff size [59], which was 7–9 atoms for all our datasets, were considered to be reliably distinguished from the random solutes, as the probability of finding these clusters in real atom probe datasets was significantly higher than that in the virtual group of randomly distributed O atoms (also shown in Fig. 5f). Thus, we propose the following empirical fitting curve for the cluster size distribution:

$$f_{CL}(N) = \exp\left[p_1 \exp\left(-\frac{N}{p_1 p_2}\right) + p_3 - \frac{N}{p_4}\right]. \quad (1)$$

$p_1, \ldots, p_4$ are fitting parameters, with $p_4 > p_2 > 0$. When N was very small, the population of clusters (f_{CL}) decreased drastically with increasing N, following an exponential

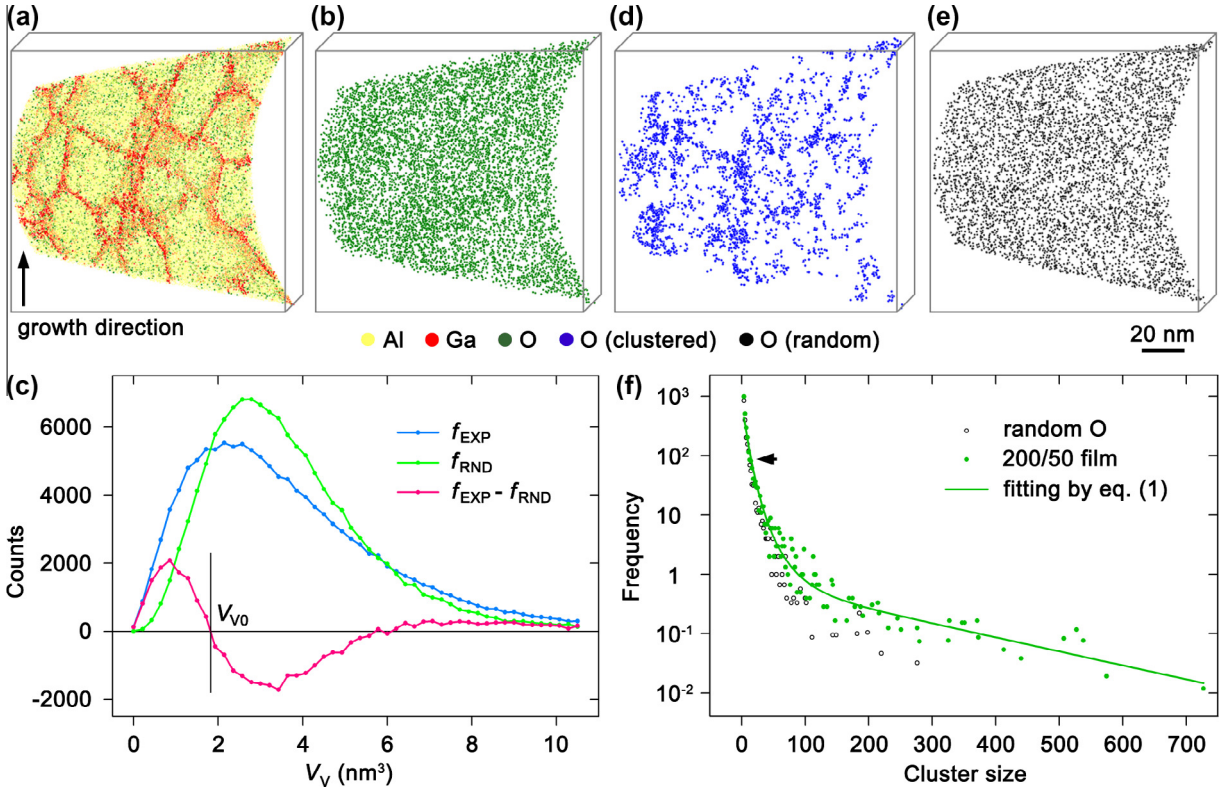

Fig. 5. 3D-APT characterization of NC Al–O thin films. (a) Reconstructed image of a typical slice with volume of 130 × 120 × 8 nm^3 from the dataset of 200/50 film. Al, O and Ga atoms are represented by yellow, green and red dots, respectively. Only 8% of Al atoms are shown for clarity. (b) Spatial distribution of all O atoms in (a). (c) Experimental Voronoi volume (V_V) distribution of all O atoms in the dataset of 200/50 film (blue curve), calculated V_V distribution of the same amount of randomly distributed O atoms (green curve), and their difference (red curve) which defines the threshold (V_{V0}) between O-rich clusters and random O solutes. (d and e) Spatial distribution of (d) O-rich clusters and (e) O solutes in (a). O atoms in clusters and solutes are represented by blue and black dots, respectively. (f) Size distribution of O-rich clusters in the dataset of 200/50 film (solid circles) and the virtual group of randomly distributed O atoms (open circles). The arrow shows the cutoff size of clusters. The fitting curve is given by Eq. (1). (For interpretation of the references to color in this figure legend, the reader is referred to the web version of this article.)

decay as in the virtual group of random solutes [59]. When N became larger, f_{CL} positively deviated from the random solutes and finally converged to a much slower exponential decay, indicating the segregation of O-rich clusters. Cluster size distributions of all datasets were well fitted using Eq. (1). For instance, $p_1 = 6.97$, $p_2 = 5.73$, $p_3 = -0.264$ and $p_4 = 184$ for a dataset of 200/50 film (see Fig. 5f). The average cluster size ($\langle N \rangle$) was then calculated based on Eq. (1) for each dataset, ranging from 25 to 33 atoms and yielding an average of 30 atoms, equivalent to a diameter of 1.4 nm if considered as α-Al_2O_3 precipitates. Moreover, individual O-rich clusters containing as many as 700 atoms (equivalent to α-Al_2O_3 precipitates with a diameter of 3.8 nm) were occasionally observed in each dataset. Thus, we suggest that the upper size limit of O-rich clusters revealed by 3D-APT has overlapped with the lower size limit of α-Al_2O_3 precipitates revealed by HRTEM. Nevertheless, α-Al_2O_3 precipitates larger than ~2 nm were observed quite rarely by 3D-APT, possibly due to the brittleness of atom probe specimens with high O content (i.e. containing large α-Al_2O_3 precipitates) and the very different emission fields between Al and α-Al_2O_3 [67].

Taken as a whole, it can be concluded by combining the results from HRTEM and 3D-APT that the O impurities were partly bounded in very small precipitates and clusters near GBs, with sizes continuously covering a range from ~10 nm to ~10 atoms, due to the strong chemical interactions of the Al–O system. The remaining O atoms were present as solid-solution inside Al grains despite the very low solubility, likely circumvented due to the far-from-equilibrium nature of sputtering deposition.

3.2. Mechanical behavior

Mechanical properties of NC Al–O thin films were primarily evaluated by means of nanoindentation operated in the CSM mode [61], which is suited to the measurement of relatively soft materials with marked indentation pile-up behavior wherein the true contact area (A) cannot be accurately determined. At each indentation depth (h), the Oliver–Pharr hardness (H) and reduced modulus (E_r) were defined as [60]:

$$H = \frac{P}{A}, \quad E_r = \frac{\sqrt{\pi}}{2\beta_i}\frac{S}{\sqrt{A}}. \tag{2}$$

Here, P and S are load and harmonic contact stiffness, respectively, and β_i is a constant determined by the geometry of indenter ($\beta_i = 1.034$ for a Berkovich tip [71]). The pile-up effects can be eliminated by writing Eq. (2) as:

$$\frac{H}{E_r^2} = \beta_i^2 \frac{4}{\pi} \frac{P}{S^2}. \quad (3)$$

Fig. 6(a) shows P/S^2 measured as functions of h/t for representative batches of films with similar t but different C_O and $\langle d_{Al} \rangle$, i.e. 200/0, 200/10, 200/50 and 200/100. All measurements shown in Fig. 6 were carried out at $\dot{\varepsilon}_i = 0.05\ s^{-1}$. As h/t increased, P/S^2 typically showed an initial dramatic decrease ($h/t < 0.5$), which may result from surface roughness and/or surface oxidation, and ended with a steady increase after the indenter reached the substrate ($h/t > 1$). Importantly, a plateau region of P/S^2 was consistently revealed for all films as h approached t. Herein, we define the plateau as $0.6 < h/t < 0.9$ (see Fig. 6a), which is similar to the results of Ref. [60] for Al films on glass substrate. Then, the averaged P/S^2 values in this range were used to determine the "true" indentation hardness (H_f) of films through:

$$H_f = \beta_i^2 \frac{4}{\pi} \cdot \left\langle \frac{P}{S^2} \right\rangle \cdot E_r^2. \quad (4)$$

Fig. 6b shows E_r measured as functions of h/t for the same batches of films as in Fig. 6a. Although the E_r values were indeed overestimated owing to pile-up effects [61], it was unambiguously revealed for all measured films that E_r firstly increased with h/t, and then rapidly converged to a constant value which is dominated by the modulus of substrate (E_s) and thus not influenced by O content. The different asymptotic limits of E_r shown in Fig. 6b are likely the artifact due to the differing extent of pile-up effects, which depend on the capacity of plastic deformation of the films, which has been shown to diminish with increasing O content [40]. In the range $0.6 < h/t < 0.9$, specifically, E_r was within 90% of its asymptotic limit and was approximately independent of h/t since the elastic properties of glass substrate matched well with Al films [60]. Therefore, we assumed that E_r in Eq. (4) was, to the first order, constant for all batches of films (in the range $0.6 < h/t < 0.9$) and can be approximated by:

$$E_r = \left(\frac{1 - \nu_i^2}{E_i} + \frac{1 - \nu_s^2}{E_s} \right)^{-1}. \quad (5)$$

The subscripts i and s stand for indenter and substrate, respectively, and E and ν are their Young's modulus and Poisson's ratio. Here we used $E_i = 1140$ GPa and $\nu_i = 0.07$ for the diamond tip, and $E_s = 73$ GPa and $\nu_s = 0.35$ for the glass substrate [60].

Fig. 7 shows H_f for all batches of films measured at $\dot{\varepsilon}_i = 0.05\ s^{-1}$. H_f generally increased with increasing C_O and decreasing $\langle d_{Al} \rangle$, which was consistent with previous studies on NC alloys [43–48] on a qualitative level. Hence, the following discussion will focus on quantitative understanding of the strengthening mechanisms, with special attention paid to separation of the multiple strengthening features attributed to the O impurities and fine grain size.

In order to provide some indication of the dominant mechanisms of deformation and strengthening, H_f were also measured at different $\dot{\varepsilon}_i$ (0.02, 0.05, 0.2 and 0.5 s^{-1}) for selected batches of films with similar t but different C_O and $\langle d_{Al} \rangle$, i.e. 200/0, 200/10, 200/50 and 200/100. As shown in Fig. 8a, H_f increased with $\dot{\varepsilon}_i$ for all measured films, with the strain-rate sensitivity ($m = \partial \ln H_f / \partial \ln \dot{\varepsilon}_i$) calculated to be 0.02–0.05. These m values in NC Al–O thin films were remarkably higher than in their coarse-grained counterparts [72] by about one order of magnitude, but were in the similar range to ultrafine-grained Al ($m = 0.01$–0.02) and NC Al films ($m = 0.03$–0.14) in previous reports [73–75]. To elucidate this variation of strain-rate dependence in further detail, the apparent activation volume (Ω^*) was evaluated based on [43,76]:

$$\Omega^* = \sqrt{3} k_B T \frac{\partial \ln \dot{\varepsilon}_i}{\partial \sigma_y} = 3\sqrt{3} k_B T \frac{\partial \ln \dot{\varepsilon}_i}{\partial H_f}. \quad (6)$$

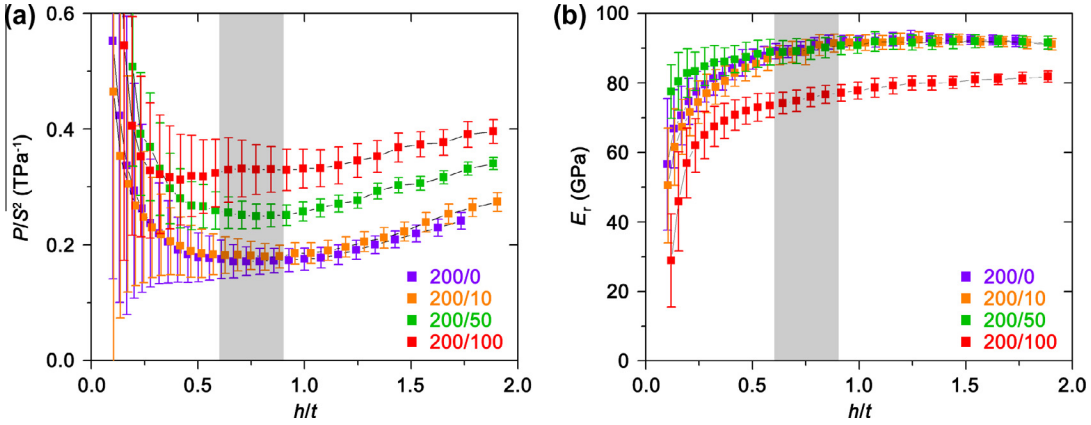

Fig. 6. Nanoindentation measurement of the mechanical properties of NC Al–O thin films. (a) P/S^2 as functions of indentation depth (h) normalized by film thickness (t) for films 200/0, 200/10, 200/50 and 200/100. Values of "true" indentation hardness are determined based on the plateaus of $0.6 < h/t < 0.9$ (shaded). (b) Oliver–Pharr reduced modulus (E_r) as functions of h/t. Error bars designate standard deviations of at least 16 measurements. (For interpretation of the references to color in this figure, the reader is referred to the web version of this article.)

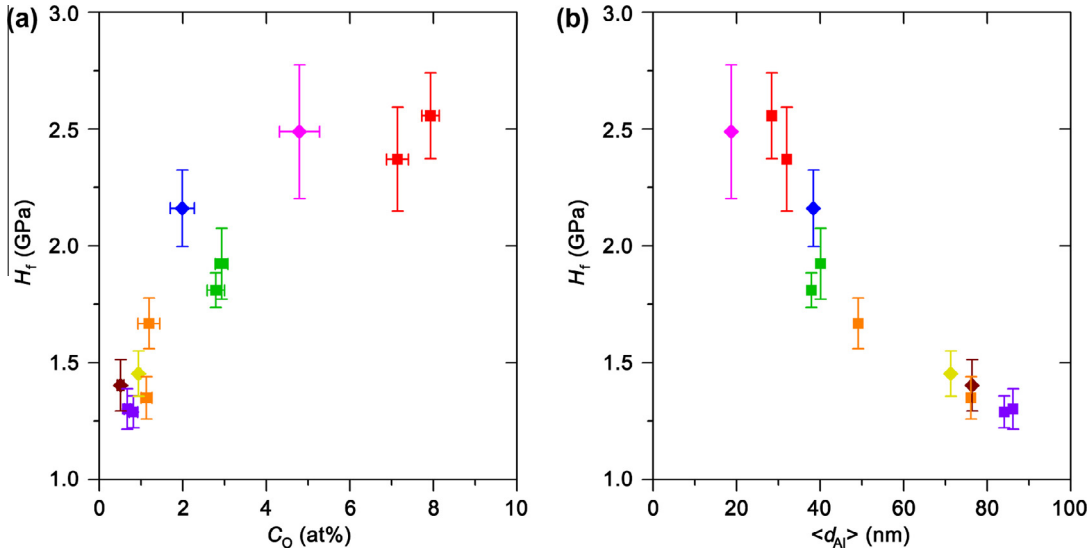

Fig. 7. Dependence of "true" indentation hardness (H_f) of NC Al–O thin films on (a) global O content (C_O) and (b) mean grain size ($\langle d_{Al}\rangle$).

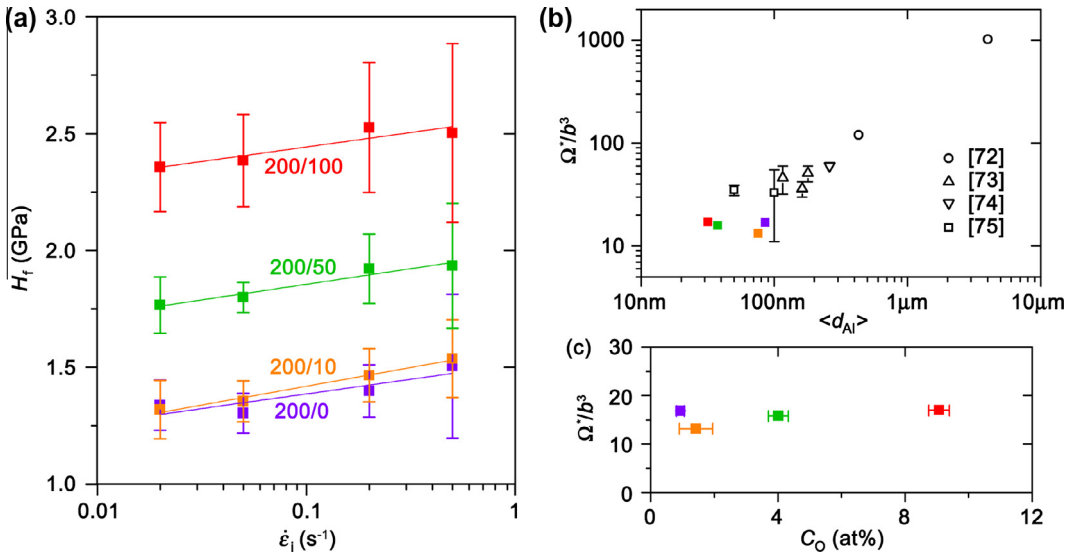

Fig. 8. Strain rate dependence of NC Al–O thin films. (a) "True" indentation hardness (H_f) measured at different indentation strain rates ($\dot{\varepsilon}_i$). (b) Dependence of activation volume (Ω^*, normalized by cubed Burgers vector b^3) on mean grain size ($\langle d_{Al}\rangle$, solid squares), compared with previous experimental results in ultrafine- and coarse-grained Al (open symbols). (c) Dependence of activation volume on global O content (C_O). (For interpretation of the references to color in this figure, the reader is referred to the web version of this article.)

Ω^* is often taken as the thermally activated signature of a rate-limited deformation mechanism. Here, k_B is the Boltzmann constant, T is temperature and is assumed to be 300 K. σ_y is the yield strength under uniaxial tension and we assume $H_f = T_1\sigma_y$ with Tabor factor $T_1 = 3$ [77]. Although T_1 was sometimes reported to be >3 in NC metals [48,78], the larger factor may result from surface defects and low density inherent to some NC films, which leads to the asymmetric tensile–compressive behavior. Stress-driven grain growth in NC films with low enough impurity content may also decrease σ_y [18] due to the early onset of microplasticity [21–23]. Overall, Ω^* were calculated to be $13b^3$–$17b^3$ (where b is the Burgers vector) for all measured films in Fig. 8a. In contrast, much larger Ω^* were reported previously in ultrafine ($40b^3$–$100b^3$) and coarse ($100b^3$–$1000b^3$) grained Al [72–74], as displayed in Fig. 8b. The decreasing Ω^* with decreasing grain size has been demonstrated in other fcc metals such as Cu [12,79] and Ni [43,76], and was believed to reflect the transition of rate-limited deformation mechanism from dislocation forest interactions inside grains to GB-related processes such as dislocation emission/absorption at GBs. Ω^* can be further decreased by solid-solution or precipitation [80,81], though this is only a higher-order effect in NC metals exhibiting very small Ω^*. On the other hand, the Ω^* values measured here were still much larger than what was predicted (b^3–$2b^3$) for "pure" GB-mediated processes such as GB sliding and shear-coupled GB migration [82,83], which

can be directly realized via short-range atomic diffusion or shuffling [27,83]. Thus we concluded that interactions between dislocations and obstacles (GBs and impurities) still played the dominant role in the strengthening of NC Al–O thin films. Most importantly for this study, Fig. 8b and c show that Ω^* was not remarkably dependent on $\langle d_{Al}\rangle$ or C_O, which suggested a consistent rate-limited mechanism despite the relatively wide-range variation of composition and microstructure over all measured films. This result thus enables a systematic modeling approach capable of delineating the strengthening contributions of various microstructural features in our films. In the following section, the physical underpinnings of our analytical model are described and the data shown in Fig. 7 can be clearly understood on a quantitative level.

4. Discussion

4.1. Modeling the strengthening behavior of NC Al–O thin films

As revealed in the above TEM and 3D-APT characterizations, O impurities in NC Al–O thin films were present as multiple morphologies including α-Al_2O_3 precipitates, O-rich clusters and random solutes. For clarity, α-Al_2O_3 precipitates are hereinafter specified as crystalline particles, which served as strong obstacles to dislocations [84]. In contrast, O-rich clusters are specified as localized regions, mostly near GBs and sometimes within Al grains, with O concentrations higher than the surrounding but not sufficiently high to precipitate. Therefore, they are considered analogous to coherent (and weak) precipitates in terms of their strengthening effect [85]. Regarding the solute atoms, their role in strengthening was simply modeled as an increase of lattice friction for dislocation slip [44,86]. As a first step to distinguishing the individual strengthening contributions from these features, the partitioning of global O content (C_O) was estimated as follows. Based on deconvolution of the bimodal grain size distribution (e.g. Fig. 2c and d), the O content contributed by α-Al_2O_3 precipitates ($C_{O\text{-}NP}$) can be determined as:

$$C_{O\text{-}NP} = \frac{\frac{3\rho_\alpha}{M_\alpha}\sum f_\alpha(\log d)\cdot d^3}{\frac{5\rho_\alpha}{M_\alpha}\sum f_\alpha(\log d)\cdot d^3 + \frac{\eta\rho_{Al}}{M_{Al}}\sum f_{Al}(\log d)\cdot d^3}. \quad (7)$$

The subscripts α and Al stand for α-Al_2O_3 precipitates and Al grains, respectively, and ρ, M and $f(\log d)$ are their density, molar weight and log-normal distribution function, respectively. $\eta = 2.3$ is the averaged aspect ratio of Al grains. Fig. 9 plots the $C_{O\text{-}NP}$ calculated for all batches of films, which generally increased with C_O, and linear fitting yields a constant partition ratio $\varphi_{NP} = C_{O\text{-}NP}/C_O = 0.27$. This linear relationship was more clearly displayed by plotting C_O vs. C_O-$C_{O\text{-}NP}$ (also shown in Fig. 9), which is equal to the O content contributed by both O-rich clusters ($C_{O\text{-}CL}$) and solute atoms ($C_{O\text{-}SS}$).

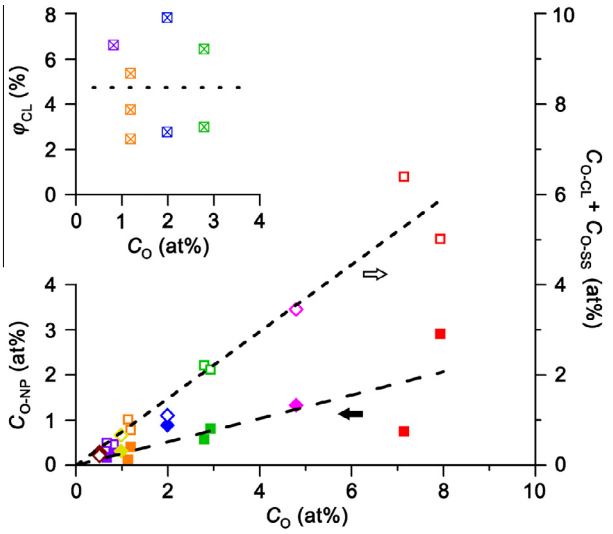

Fig. 9. Partition of global O content (C_O) in the multiple chemical states of O impurities. Solid symbols and dashed line: O content in α-Al_2O_3 precipitates ($C_{O\text{-}NP}$) measured by grain size distribution in TEM; open symbols and short dashed line: sum of O contents in O-rich clusters ($C_{O\text{-}CL}$) and solute atoms ($C_{O\text{-}SS}$), which equals to C_O–$C_{O\text{-}NP}$; crossed symbols and dotted line: $\varphi_{CL} = C_{O\text{-}CL}/C_O$ measured by cluster analysis in 3D-APT. (For interpretation of the references to color in this figure, the reader is referred to the web version of this article.)

$C_{O\text{-}CL}$ and $C_{O\text{-}SS}$ can be further separated by means of 3D-APT and V_V distribution analyses. Since α-Al_2O_3 precipitates were rarely observed in atom probe specimens, we assume that the segregated O atoms, corresponding to $I_{DIFF} = \int_0^{V_{V0}}(f_{EXP} - f_{RND})dV_V$ (see Fig. 5c), consisted exclusively of O-rich clusters. Meanwhile, the O content measured by 3D-APT, corresponding to $I_{EPR} = \int_0^{+\infty} f_{EXP}dV_V$, was always lower than the global O content also because high-O regions containing α-Al_2O_3 precipitates were not effectively sampled. Therefore, the C_O measured by EDS were used in following quantitative analysis, and the partition ratio for O-rich clusters, i.e. $\varphi_{CL} = C_{O\text{-}CL}/C_O = (1-\varphi_{NP})I_{DIFF}/I_{EXP}$, was calculated for each atom probe datasets, giving an averaged value of 0.05 (see inset of Fig. 9). Although only a few datasets were measured, φ_{CL} was reasonably assumed constant. As a result, $\varphi_{SS} = C_{O\text{-}SS}/C_O = 1 - \varphi_{NP} - \varphi_{CL} = 0.68$ was also constant, which naturally leads to the approximation that the global C_O was proportionally partitioned according to the multiple morphological states of impurities.

Having obtained a quantitative picture of the full microstructure of NC Al–O thin films, the strengthening effects of individual impurity features were then derived based on the well-established theories of interactions between dislocations and obstacles [84–86]. First, α-Al_2O_3 precipitates were considered as very strong obstacles, forcing dislocations to circumvent them as in the Orowan mechanism [84,87]. However, we note the mean spacing between precipitates, estimated as $\langle d_{NP}\rangle \upsilon_{NP}^{-1/3}$ (υ_{NP} is the volume fraction of precipitate, and simple math following Eq. (7) gives $\upsilon_{NP} = (\rho_{Al}M_\alpha/3\rho_\alpha M_{Al})C_{O\text{-}NP} = 0.87\varphi_{NP}C_O$), was of

the same order of $\langle d_{Al}\rangle$ for all batches of films. This is different from some reports on dispersoid strengthening in nanostructured metals [54,87], in which oxide precipitates were dispersed with mean spacings substantially smaller than grain sizes. We thus assume that α-Al_2O_3 precipitates were preferentially located on the Al GBs, which would also be expected as energetically favorable nucleation sites for large (and incoherent) precipitates [30]. As a result, each dislocation emitted from GBs [21,26] would be subsequently pinned (at either or both ends) by the α-Al_2O_3 precipitates residing on GBs, with the maximum bowing curvature effectively limited by $\langle d_{Al}\rangle$. The increase of critical shear stress due to dislocation bowing was thus modeled as:

$$\Delta\tau_{NP} = \beta_{NP}\beta_{\sigma}\frac{Gb}{\langle d_{Al}\rangle}. \quad (8)$$

Here, G is shear modulus, b is Burgers vector, $\beta_{NP} = 0.84$ for very strong obstacles [84,88], and $\beta_{\sigma} = 0.38$ is given by the standard deviation of grain size distributions following the Pythagorean sum rule, which was shown to be optimal for the superposition of strengthening produced by obstacles with similar strengths [89,90]. We note that the critical shear stress for dislocation nucleation from GBs showed the same scaling of $\langle d_{Al}\rangle^{-1}$, which was suggested to prevail over the H–P relationship as grain sizes were refined to the nanoscale [2,91], and the corresponding Ω^* as small as $10b^3$–$20b^3$ [76,79] also accorded well with our measurements (see Fig. 8). Thus, Eq. (8) integrated the strengthening effects contributed by driving dislocations through nanosized grains and the subsequent pinning by α-Al_2O_3 precipitates. The increase of H_f was thus written as $\Delta H_{f\text{-}NP} = T_1T_2\Delta\tau_{NP}$, with Tabor factor $T_1 = 3$ [77] and Taylor factor $T_2 = 3.06$ [30].

As stated above, the O-rich clusters were considered as coherent particles, since their lattice constant was slightly different from the Al matrix due to the higher concentration of O atoms, which can be simply considered as supersaturated solid-solution. The interactions between dislocations and the misfit strain field around clusters thus lead to an additional strengthening effect [85], though weaker than that caused by the hard α-Al_2O_3 precipitates. Accordingly, dislocations were expected to cut through these clusters, irrespective of whether they were located on GBs or inside grains. The change of elastic modulus due to O solid-solution also contributed to strengthening, but was much weaker than the size misfit effect [85,92]. The increase of H_f due to O-rich clusters was thus expressed as [92]:

$$\Delta H_{f\text{-}CL} = T_1T_2\Delta\tau_{CL} = \beta_{CL}T_1T_2G\varepsilon_{CL}^{\frac{3}{2}}\left(\frac{\langle d_{CL}\rangle}{b}\right)^{\frac{1}{2}}\upsilon_{CL}^{\frac{1}{2}}. \quad (9)$$

Here, ε_{CL} is the misfit strain between O-rich clusters and Al matrix, $\langle d_{CL}\rangle$ is the average diameter of clusters, and υ_{CL} is the volume fraction of clusters. The constant $\beta_{CL} = 9.6$ is determined by the shape of the dislocation stress field and the Poisson ratio of Al [92]. As calculated based on Eq. (1), the average size ($\langle N\rangle$) of O-rich clusters was 30 atoms, equivalent to $\langle d_{CL}\rangle \approx 1.4$ nm if considered as dense α-Al_2O_3 precipitates (note that V_V of O atoms in α-Al_2O_3 is only 0.043 nm^3). However, the averaged Voronoi volume ($\langle V_V\rangle$) for the O atoms classified as clusters was as large as 1.5 nm^3 (averaging all datasets), which means the O concentration in clusters is still much lower than in precipitates. Thus we make the following straightforward assumptions:

$$\varepsilon_{CL} = \varepsilon_M\frac{V_{WS}}{\langle V_V\rangle}, \quad \langle d_{CL}\rangle = \left(\frac{6\langle N\rangle}{\pi}\langle V_V\rangle\right)^{\frac{1}{3}},$$
$$\upsilon_{CL} = \varphi_{CL}C_O\frac{\langle V_V\rangle}{V_{WS}}. \quad (10)$$

Here, εM is the misfit strain of inserting an individual O atom (or ion) into the Wigner–Seitz cell of fcc-Al with volume VWS = 0.017 nm3. The lower and upper bounds of εM were estimated to be 0.036 and 0.58, corresponding to inserting an uncharged O atom (r = 0.66 Å) and an O2− ion (r = 1.40 Å) in the octahedral interstitial site (r = 0.59 Å) of fcc-Al lattice [93], respectively, and an experimental estimation of εM is provided below. Again, although the value of ⟨dCL⟩ = 4.3 nm determined by Eq. (10) is quite close to the sizes of the α-Al2O3 precipitates, the strengthening effect of an individual O-rich cluster is still weaker due to the larger ⟨VV⟩ of supersaturated O solutes.

Similar to but even weaker than O-rich clusters, the strengthening effect of random solute atoms was described using Labusch's theory [86] by considering the interaction between dislocations and the misfit strain field produced by an array of point defects. Again, the contribution from modulus misfit was weaker and thus neglected [92]. Since the octahedral interstitial sites in fcc-lattice are spherically symmetric, the analytical approach for substitutional solute atoms in Ref. [92] can be still applicable. The increase of H_f due to random solid-solution was thus written as:

$$\Delta H_{f\text{-}SS} = T_1T_2\Delta\tau_{SS} = \beta_{SS}T_1T_2G\varepsilon_M^{\frac{4}{3}}\varphi_{SS}^{\frac{2}{3}}\cdot C_O^{\frac{2}{3}}. \quad (11)$$

The constant $\beta_{CL} = 0.24$ is determined by the effective amplitude and width of the misfit strain field [92]. As illustrated in Fig. 10a, interactions between dislocations and the multiple states of impurities are expected to occur simultaneously, thus the measured H_f of NC Al–O thin films must be the superposition of above strengthening mechanisms following some specific sum rule. Observing that the characteristic length scales and resistances of α-Al_2O_3 precipitates (and GBs), O-rich clusters and random solutes were substantially different, here we assume the following linear superposition of their individual contributions [84,94]:

$$H_f(C_O, \langle d_{Al}\rangle) = H_0 + \kappa_{NP}\cdot\langle d_{Al}\rangle^{-1} + \chi_{CL}\cdot C_O^{\frac{1}{2}} + \omega_{SS}\cdot C_O^{\frac{2}{3}}. \quad (12)$$

The fitting parameters were analytically expressed as follows:

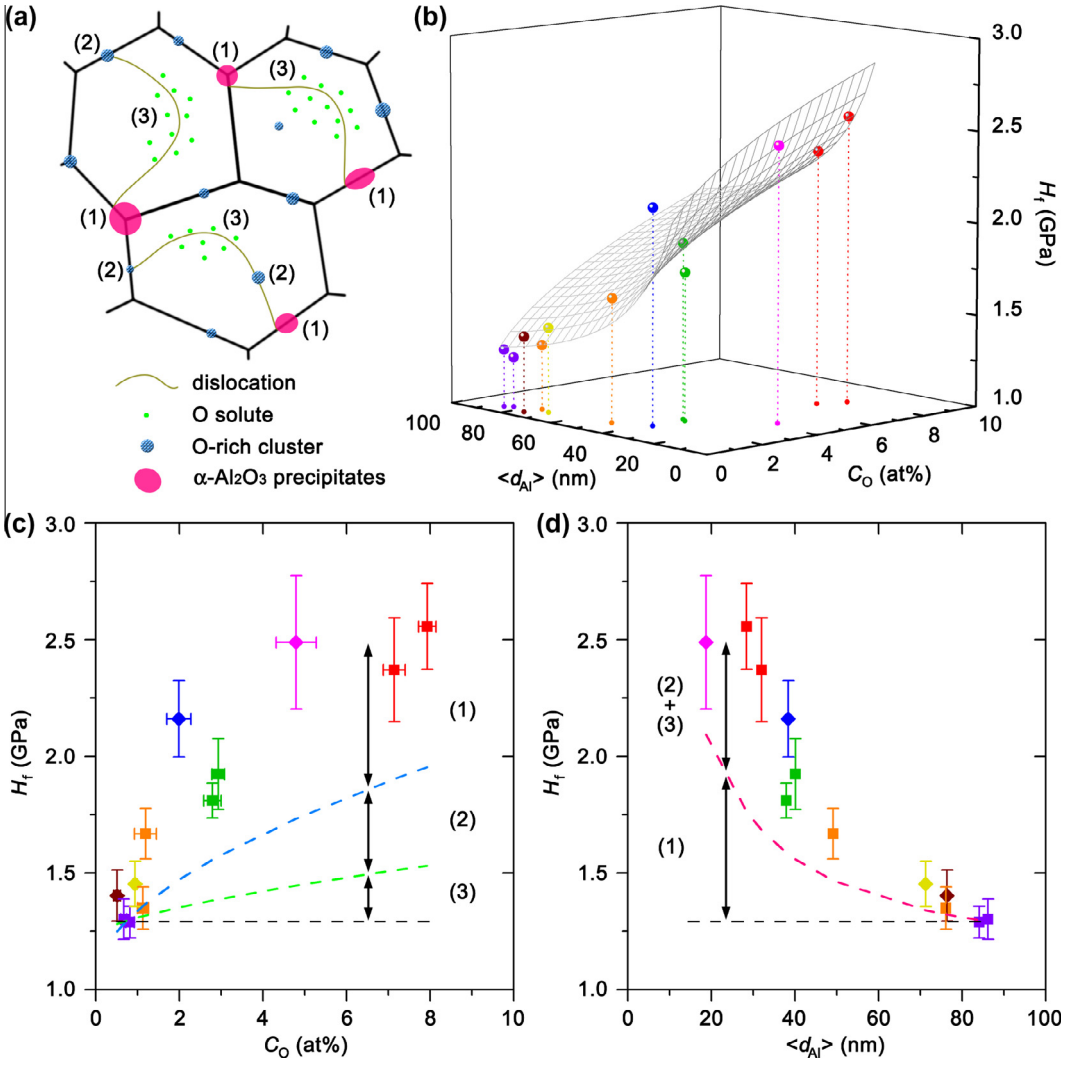

Fig. 10. Strengthening model of NC Al–O thin films. (a) Schematic of dislocation interactions with (1) α-Al_2O_3 precipitates, (2) O-rich clusters and (3) solute atoms. See text for details. (b) 3-D fitting of experimental data in Fig. 7. (c and d) Deconvolution of strengthening effects contributed by the multiple morphologies of O impurities. (For interpretation of the references to color in this figure, the reader is referred to the web version of this article.)

$$\begin{aligned}\kappa_{NP} &= 0.32T_1T_2Gb\\ \chi_{CL} &= 0.0093T_1T_2G\varepsilon_M^{\frac{3}{2}}\\ \omega_{SS} &= 0.0086T_1T_2G\varepsilon_M^{\frac{4}{3}}\end{aligned}. \tag{13}$$

The experimental results in Fig. 7 were well fitted by Eq. (12) for the full space of C_O and $\langle d_{Al}\rangle$, yielding fitting parameters $H_0 = 0.86$ GPa, $\kappa_{NP} = 19.9$ GPa nm, $\chi_{CL} = 0.22$ GPa and $\omega_{SS} = 0.075$ GPa (see Fig. 10b). Using $T_1 = 3$, $T_2 = 3.06$, and the values of bulk Al, i.e. $G = 26$ GPa and $b = 0.286$ nm, yielded $\kappa_{NP} = 21.8$ GPa nm, which agrees quantitatively with the fitted value. The result was still reasonable even when using $T_1 > 3$, which can be reconciled by considering the moduli of NC Al–O thin films to be lower than bulk values, as suggested by several measurements of NC thin films [48,95,96]. In addition, the fitted value of κ_{NP} can be used for the evaluation of other parameters, since the term T_1T_2G was common to all strengthening contributions. Based on Eq. (13), the atomic misfit strain ε_M was calculated as 0.10–0.21, corresponding to an O atomic radius of 0.78–0.95 Å, which indicated a substantial charge transfer between the interstitial O atom and the surrounding Al lattice, as predicted by previous atomistic simulations [42].

Hence, the individual contributions from each of the strengthening features were well separated, as shown in Fig. 10c and d. We show that both O impurities and grain size contributed remarkably to the strengthening of NC Al–O thin films. Moreover, α-Al_2O_3 precipitates (coupled with GBs) served as the principal strengthening features due to their strong resistance to dislocations. The strengthening effect of O-rich clusters was nearly comparable to that of α-Al_2O_3 precipitates due to the large number of supersaturated fine regions, even though the resistance of individual clusters is moderate. This non-negligible strengthening contribution from O-rich clusters further motivates the need for systematic characterization of such complex microstructures, which cannot be adequately represented by conventional TEM approaches alone. Finally,

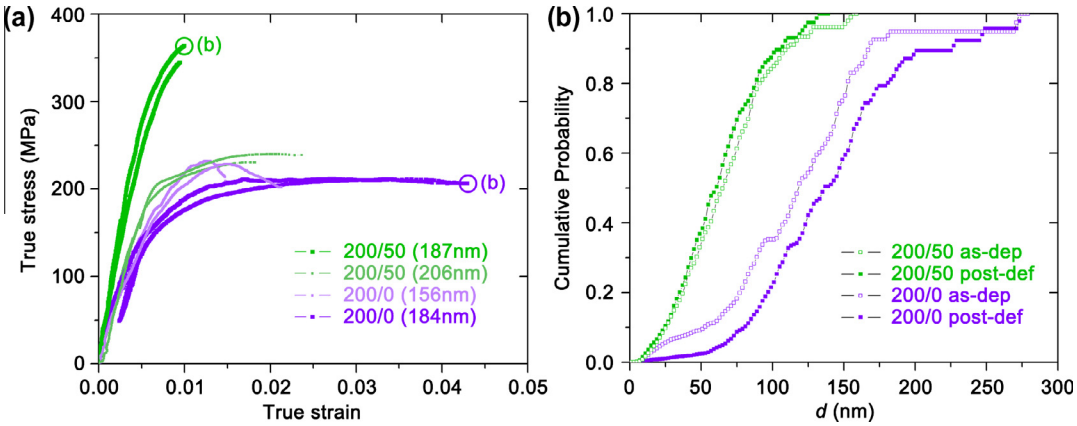

Fig. 11. Microtensile testing of NC Al–O thin films. (a) Stress–strain curves for films 200/0 and 200/50 (two batches each, with different film thickness). (b) Comparison of grain size statistics (area-weighted cumulative probability) measured in as-deposited (as-dep) films and close to fracture end of post-deformed (post-def) films. (For interpretation of the references to color in this figure, the reader is referred to the web version of this article.)

solid–solution strengthening was found to be much weaker in NC Al–O thin films, thus re-emphasizing the significance of strong chemical interactions, which are particularly important in the Al–O system, for the mechanical properties of NC alloys.

4.2. Tailoring the mechanical behavior of NC Al–O thin films

Whereas the above analysis focused on the hardening mechanisms of NC Al–O thin films, we now turn attention to the overall mechanical behavior of these materials as measured by microtensile testing. Fig. 11a shows representative true stress–true strain behavior measured from two batches of 200/0 and two batches of 200/50 films. As indicated, the film thicknesses varied between the batches of each nominal composition. The following salient features can be identified from these microtensile curves and the strength and ductility values listed in Table 1. First, the 200/0 films show very low yield strengths and moderate ultimate strengths. The thinner films ($t = 156$ nm) showed lower ductility, an effect that has been previously reported [18,75] and discussed in the context of the role of specimen geometry on governing necking instabilities and thus uniform plastic deformation. Nonetheless, the tensile behavior of both 200/0 films (e.g. early deviation from linear elasticity, relatively large plastic strain) is reminiscent of the mechanical response of sufficiently pure NC films undergoing stress-driven grain growth [18,40]. Indeed, measurement of grain size distributions before and after tensile test (see Fig. 11b) reveals microstructural evolution owing to the applied deformation.

In contrast, the 200/50 films demonstrated elevated strengths and reduced tensile ductility. The effect of addition of O impurities can be clearly seen by comparing the 200/0 and 200/50 films with near-identical thicknesses (184 and 187 nm, respectively). Interestingly, the thicker 200/50 films ($t = 206$ nm) showed total strains to failure as high as 2%, demonstrating a capacity for plastic deformation even in films with small grain sizes and relatively high impurity contents. These films also showed a sharp transition from an apparent elastic to a plastic regime, which is suggestive of an increase in the overall pinning strength of impurities needed for plastic flow compared to microplasticity. Unlike the 200/0 films, the 200/50 films showed no stress-driven grain growth, as indicated by the grain size statistics shown in Fig. 11b. This result corroborates the work of Tang et al. [40], who proposed that a critical GB excess of O solutes was required to suppress the stress-driven microstructural evolution. Therefore, the O content available in 200/50 films was sufficient to pin GBs from large-scale migration, while the 200/0 films were effectively pure, though α-Al_2O_3 precipitates and O-rich clusters were still present. The grain growth mechanisms have been shown to produce plastic strain [97,98], but the present results suggest that alternate mechanisms are responsible for tensile ductility in NC alloy films where grain growth is largely suppressed. Nevertheless, our above model for hardening relies only on the initial microstructural parameters, whereas any description of late-stage flow behavior or damage accumulation would need to account for microstructural evolution during deformation. Taken as a whole, the complex microstructures with various chemical and structural states of O impurities lead to a wide range of mechanical behavior, all of which show different extents of plastic deformation.

5. Conclusions

On the basis of quantitative microstructural characterization, mechanical behavior measurements and analytical modeling of NC Al–O thin films, we draw the following conclusions:

- Our confocal co-sputtering approach enables the microstructure and mechanical behavior of NC Al–O thin films to be studied over a wide range of grain sizes and compositions. The global O content and mean grain sizes were controlled by DC and RF power in a quasi-independent manner.

- Multiple morphologies of O impurities, including nanosized α-Al_2O_3 precipitates, O-rich clusters segregated along GBs, and O solutes randomly dispersed within Al grains, were revealed by detailed HRTEM and 3D-APT characterization. Quantification of O content in each feature was further enabled by analyses of grain size statistics and Voronoi volume distributions, indicating constant partition ratios of the global O content over the entire composition range.
- The hardness of NC Al–O thin films was found to depend strongly on both grain size and composition, and increased by nearly a factor of 2 for very fine grain sizes and high O contents relative to purer counterparts. Moreover, the hardness was found to be strongly rate sensitive, with apparent activation volumes of $13b^3$–$17b^3$, which were consistent over the entire grain size and composition range, suggesting the same rate-limited deformation mechanism(s) in all the films studied.
- The strengthening of NC Al–O thin films was well delineated only when considering both impurity and grain size effects. A microstructure-informed analytical model was able to capture the strengthening behavior over the full range of grain size and O content, and the contributions from each strengthening feature could be distinguished. Our model indicated that α-Al_2O_3 precipitates and O-rich clusters played dominant roles, while random solute atoms played only a secondary role.
- Microtensile testing of selected batches of NC Al–O thin films showed similar trends in strengthening and a capacity for ductile behavior in both nominally pure and alloyed films. Stress-driven grain growth was found to be suppressed in higher O content films, highlighting the role of impurity atmosphere in pinning GBs from migration induced by local stresses.

Our study as a whole demonstrates the diversity of mechanical behavior that results from the combination of chemical and structural features with nanoscale dimensions. In comparison to other reported NC alloy systems with more typical metallic bonding between constituent species, NC Al–O thin films show greatly enhanced strengthening capability over a modest composition range, thus underlining the role of strong chemical interactions in our Al–O system and the various microstructures that can be consequently obtained. The relative efficacy of nanocrystalline grain sizes, nanoscale precipitates, and supersaturated solid solution in controlling other important structural and functional properties such as thermal stability, thermal conductivity and thermoelectricity, should be interesting avenues for future research.

Acknowledgements

This work is supported by the National Science Foundation (NSF) Materials Network Program (Grant Nos. DMR-1008222 and DMR-1008156) and the Australian Research Council (ARC). D.S.G. acknowledges additional support through start-up funding from the University of Pennsylvania. F.G. acknowledges additional technical support from Agilent Technologies. The authors are grateful for scientific and technical input and support from the Penn Nanoscale Characterization Facility (NCF) and the Australian Microscopy & Microanalysis Research Facility (AMMRF) node at the University of Sydney.

References

[1] Kumar KS, Van Swygenhoven H, Suresh S. Acta Mater 2003;51:5743.
[2] Dao M, Lu L, Asaro RJ, De Hosson JTM, Ma E. Acta Mater 2007;55:4041.
[3] Lu L, Chen X, Huang X, Lu K. Science 2009;323:607.
[4] Wu XL, Zhu YT, Wei YG, Wei Q. Phys Rev Lett 2009;103:205504.
[5] Wang YM, Chen MW, Zhou FH, Ma E. Nature 2002;419:912.
[6] Legros M, Gianola DS, Hemker KJ. Acta Mater 2008;56:3380.
[7] Roy I, Yang HW, Dinh L, Lund I, Earthman JC, Mohamed FA. Scripta Mater 2008;59:305.
[8] Padilla II HA, Boyce BL. Exp Mech 2010;50:5.
[9] Rupert TJ, Schuh CA. Acta Mater 2010;58:4137.
[10] Schiøtz J, Jacobsen KW. Science 2003;301:1357.
[11] Schuh CA, Nieh TG, Iwasaki H. Acta Mater 2003;51:431.
[12] Cheng S, Ma E, Wang YM, Kecskes LJ, Youssef KM, Koch CC, et al. Acta Mater 2005;53:1521.
[13] Chen MW, Ma E, Hemker KJ, Sheng HW, Wang YM, Cheng XM. Science 2003;300:1275.
[14] Budrovic Z, Van Swygenhoven H, Derlet PM, Van Petegem S, Schmitt B. Science 2004;304:273.
[15] Shan ZW, Stach EA, Wiezorek JMK, Knapp JA, Follstaedt DM, Mao SX. Science 2004;305:654.
[16] Jin M, Minor AM, Stach EA, Morris JW. Acta Mater 2004;52:5381.
[17] Zhang K, Weertman JR, Eastman JA. Appl Phys Lett 2005;87:061921.
[18] Gianola DS, Van Petegem S, Legros M, Brandstetter S, Van Swygenhoven H, Hemker KJ. Acta Mater 2006;54:2253.
[19] Rupert TJ, Gianola DS, Gan Y, Hemker KJ. Science 2009;326:1686.
[20] Boyce BL, Padilla II HA. Metall Mater Trans A 2011;42:1793.
[21] Mompiou F, Legros M, Boé A, Coulombier M, Raskin JP, Pardoen T. Acta Mater 2013;61:205.
[22] Kobler A, Kashiwar A, Hahn H, Kübel C. Ultramicroscopy 2013;128:68.
[23] Lohmiller J, Baumbusch R, Kraft O, Gruber PA. Phys Rev Lett 2013;110:066101.
[24] Yamakov V, Wolf D, Phillpot SR, Mukherjee AK, Gleiter H. Nat Mater 2004;3:43.
[25] Cahn JW, Taylor JE. Acta Mater 2004;52:4887.
[26] Van Swygenhoven H, Derlet PM, Frøseth AG. Acta Mater 2006;54:1975.
[27] Cahn JW, Mishin Y, Suzuki A. Acta Mater 2006;54:4953.
[28] Velasco M, Van Swygenhoven H, Brandl C. Scripta Mater 2011;65:151.
[29] Schäfer J, Albe K. Acta Mater 2012;60:6076.
[30] Abbaschian R, Abbaschian L, Reed-Hill RE. Physical metallurgy principles. Stamford, CA: Cengage Learning; 2009.
[31] Cahn JW. Acta Metall 1962;10:789.
[32] McLean D. Grain boundaries in metals. London: Oxford University Press; 1957.
[33] Weissmuller J. Nanostruct Mater 1993;3:261.
[34] Trelewicz JR, Schuh CA. Phys Rev B 2009;79:094112.
[35] Chookajorn T, Murdoch HA, Schuh CA. Science 2012;337:951.
[36] Choi P, da Silva M, Klement U, Al-Kassab T, Kirchheim R. Acta Mater 2005;53:4473.
[37] Frolov T, Darling KA, Kecskes LJ, Mishin Y. Acta Mater 2012;60:2158.

[38] Soer WA, De Hosson JTM, Minor AM, Morris JW, Stach EA. Acta Mater 2004;52:5783.
[39] Fan GJ, Fu LF, Choo H, Liaw PK, Browning ND. Acta Mater 2006;54:4781.
[40] Tang F, Gianola DS, Moody MP, Hemker KJ, Cairney JM. Acta Mater 2012;60:1038.
[41] Gianola DS, Mendis BG, Cheng XM, Hemker KJ. Mater Sci Eng A 2008;483–484:637.
[42] Elsener A, Politano O, Derlet PM, Van Swygenhoven H. Acta Mater 2009;57:1988.
[43] Rupert TJ, Trenkle JC, Schuh CA. Acta Mater 2011;59:1619.
[44] Fleischer RL. Solid–solution hardening. In: Peckner D, editor. The strengthening of metals. New York: Reinhold; 1964.
[45] Shen TD, Koch CC. Acta Mater 1996;44:753.
[46] Özerinç S, Tai KP, Vo NQ, Bellon P, Averback RS, King WP. Scripta Mater 2012;67:720.
[47] Mukai T, Suresh S, Kita K, Sasaki H, Kobayashi N, Higashi K, et al. Acta Mater 2003;51:4197.
[48] Gianola DS, Lee Z, Ophus C, Luber EJ, Mitlin D, Dahmen U, et al. Acta Mater 2012;61:1432.
[49] Vo NQ, Schäfer J, Averback RS, Albe K, Ashkenazy Y, Bellon P. Scripta Mater 2011;65:660.
[50] Mehta SC, Smith DA, Erb U. Mater Sci Eng A 1995;204:227.
[51] Jeong DH, Erb U, Aust KT, Palumbo G. Scripta Mater 2003;48:1067.
[52] Musil J, Jílek R, Meissner M, Tölg T, Čerstvý R. Surf Coat Technol 2012;206:4230.
[53] Odette GR, Alinger MJ, Wirth BD. Annu Rev Mater Res 2008;38:471.
[54] Liu G, Zhang GJ, Jiang F, Ding XD, Sun YJ, Sun J, et al. Nat Mater 2013;12:344.
[55] Rajagopalan J, Saif MTA. J Mater Res 2011;26:2826.
[56] Felfer P, Alam T, Ringer SP, Cairney JM. Microsc Res Tech 2012;75:484.
[57] Gault B, Haley D, de Geuser F, Moody MP, Marquis EA, Larson DJ, et al. Ultramicroscopy 2011;111:448.
[58] 3Depict. <http://threedepict.sourceforge.net>.
[59] Felfer P, Ceguerra A, Ringer SP, Cairney JM. Unpublished.
[60] Saha R, Nix WD. Acta Mater 2002;50:23.
[61] Oliver WC, Pharr GM. J Mater Res 2004;19:3.
[62] Gianola DS, Eberl C. JOM-J Miner Met Mater Soc 2009;61:24.
[63] Roberts S, Dobson PJ. Thin Solid Films 1986;135:137.
[64] Liu F, Kirchheim R. J Cryst Growth 2004;264:385.
[65] Mitra R, Hoffman RA, Madan A, Weertman JR. J Mater Res 2004;16:1010.
[66] Detor AJ, Miller MK, Schuh CA. Philos Mag 2006;86:4459.
[67] Marquis EA, Hyde JM. Mater Sci Eng, R 2010;69:37.
[68] Moody MP, Tang F, Gault B, Ringer SP, Cairney JM. Ultramicroscopy 2011;111:493.
[69] Sigle W, Richter G, Ruehle M, Schmidt S. Appl Phys Lett 1999;89:121911.
[70] Thomson DI, Heine V, Payne MC, Marzari N, Finnis MW. Acta Mater 2000;48:3623.
[71] King RB. Int J Solids Struct 1987;23:1657.
[72] May J, Höppel HW, Göken M. Scripta Mater 2005;53:189.
[73] Hayes RW, Witkin D, Zhou F, Lavernia EJ. Acta Mater 2004;52:4259.
[74] Kalkman AJ, Verbruggen AH, Radelaar S. J Appl Phys 2002;92:6612.
[75] Gianola DS, Warner DH, Molinari JF, Hemker KJ. Scripta Mater 2006;55:649.
[76] Wang YM, Hamza AV, Ma E. Acta Mater 2006;54:2715.
[77] Tabor D. The hardness of metals. New York: Oxford University Press; 2000.
[78] Dalla Torre F, Van Swygenhoven H, Victoria M. Acta Mater 2002;50:3957.
[79] Wei Q, Cheng S, Ramesh KT, Ma E. Mater Sci Eng A 2004;381:71.
[80] Diak BJ, Saimoto S. Mater Sci Eng A 1997;234–236:1019.
[81] Dong Y, Nogaret T, Curtin WA. Metall Mater Trans A 2010;41:1954.
[82] Conrad H, Narayan J. Scripta Mater 2000;42:1025.
[83] Rajabzadeh A, Mompiou F, Legros M, Combe N. Phys Rev Lett 2013;110:265507.
[84] Ardell AJ. Metall Trans A 1985;16:2131.
[85] Gleiter H, Hornbogen E. Mater Sci Eng 1967;2:285.
[86] Labusch R. Phys Status Solidi B 1970;41:659.
[87] Williams JR, Clarke DR. Acta Mater 2008;56:1813.
[88] Hanson K, Morris JW. J Appl Phys 1975;46:983.
[89] Koppenaal TJ, Kuhlmann-Wilsdorf D. Appl Phys Lett 1964;4:59.
[90] Hanson K, Morris JW. J Appl Phys 1975;46:2378.
[91] Cheng S, Spencer JA, Milligan WW. Acta Mater 2003;51:4505.
[92] Argon AS. Strengthening mechanisms in crystal plasticity. Oxford: Oxford University Press; 2008.
[93] Kittel C. Introduction to solid state physics. New York: Wiley; 1996.
[94] Kocks UF, Argon AS, Ashby MF. Thermodynamics and kinetics of slip. Oxford: Pergamon Press; 1975.
[95] Haque MA, Saif MTA. Proc Natl Acad Sci USA 2004;27:6335.
[96] Kim JH, Nizami A, Hwangbo Y, Jang B, Lee HJ, Woo CS, et al. Nat Commun 2013;4:2520.
[97] Gianola DS, Eberl C, Cheng XM, Hemker KJ. Adv Mater 2008;20:303.
[98] Gianola DS, Farkas D, Gamarra M, He MR. J Appl Phys 2012;112:124313.